DRAFT
CMS Paper

The content of this note is intended for CMS internal use and distribution only

2019/02/22
Archive Hash: d95bc50
Archive Date: 2019/02/22

Measurement of differential cross section for single top quark production in association with a W boson at $\sqrt{s} = 13\,\text{TeV}$

The CMS Collaboration

Abstract

A measurement of the differential cross section in the process where a single top quark is produced in association with a W boson is presented in proton-proton collisions at $\sqrt{s} = 13\,\text{TeV}$ in dilepton events. The fiducial region is defined according to the detector acceptance cuts, and requiring the presence of exactly one jet, that must be b-tagged. The presence of lower energy jets is vetoed to reduce the contribution from the dominating backgrounds. Resulting distributions are unfolded to particle level.

1 Introduction

Electroweak production of single top quarks has been first observed by the D0 [1] and CDF [2] Collaborations at the Fermilab Tevatron. Single top quark are produced via three processes: the exchange of a virtual W boson (t channel), the production and decay of a virtual W boson (s channel), and the associated production of a top quark and a W boson (tW channel). The latter, which has a negligible production cross section in proton-antiproton collisions at the Tevatron, represents a significant contribution to single top quark production in proton-proton (pp) collisions at the Large Hadron Collider (LHC). The study of the tW process not only provides a unique opportunity to further understand the standard model (SM) and its extensions through the interference of the process at next-to-leading order (NLO) with top quark pair ($\mathrm{t\bar{t}}$) production [3–5], but it also plays an important role because of its sensitivity to the physics beyond the SM [6–8].

The cross section for tW production is computed at an approximate next-to-next-to-leading order (NNLO). The theoretical prediction in pp collisions at $\sqrt{s} = 13\,\mathrm{TeV}$, for a top quark mass ($m_\mathrm{t}$) of 172.5 GeV, is $\sigma_{\mathrm{tW}} = 71.7 \pm 1.8\,(\mathrm{scale}) \pm 3.4\,(\mathrm{PDF})\,\mathrm{pb}$ [9]. The first uncertainty refers to the factorization (μ_F) and renormalization (μ_R) scales in quantum chromodynamics (QCD), and the second to parton distribution functions (PDFs). This value includes the charge-conjugate modes. The leading-order (LO) Feynman diagrams for tW production are shown in Fig. 1.

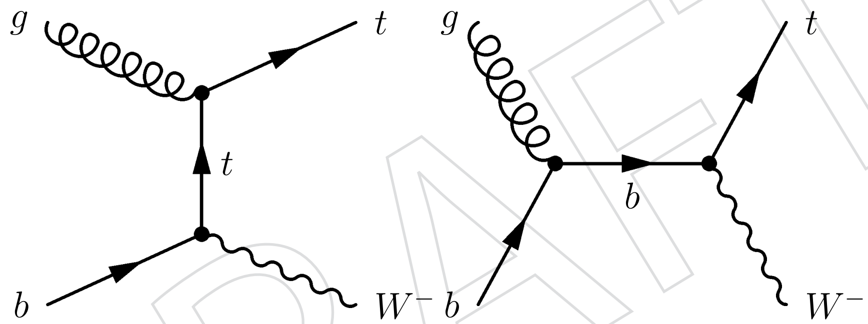

Figure 1: Leading order Feynman diagrams for single top quark production in the tW mode, the charge-conjugate modes are implicitly included.

The CMS and ATLAS Collaborations have presented evidence for [10, 11] and observations of [12, 13] this process in pp collisions at $\sqrt{s} = 7$ and 8 TeV, respectively. Using 13 TeV data, the inclusive tW production cross section has also been measured by both CMS [14] and ATLAS [15] Collaborations with accuracies of the order of 10% and 30%, respectively.

The measurement of the differential cross section is particularly challenging because of the overwhelming presence of $\mathrm{t\bar{t}}$ in the most signal-enriched region. The first attempt to measure the differential cross section of the tW production process has been performed by the ATLAS Collaboration [16], a cut-based analysis is performed in a signal-enriched region defined by a cut on a multivariate discriminant. This paper reports the first measurement of the differential cross section for tW production in CMS. The measurement uses data recorded during 2016, corresponding to an integrated luminosity of $\mathcal{L} = 35.9 \pm 0.9\,\mathrm{fb}^{-1}$. The analysis is performed using the $\mathrm{e}^{\pm}\mu^{\mp}$ dilepton channel, in which both W bosons, either produced in association with the top quark or from the decay of the top quark, decay leptonically into a muon or an electron, and a neutrino. Events with W bosons decaying into τ leptons that decay into electrons or muons also contribute to the measurement. The primary background to tW production in this final state comes from $\mathrm{t\bar{t}}$ production, with Drell–Yan (DY) production of τ lepton pairs that decay leptonically being the next most significant background. The measurement is performed over a fiducial region enriched in the signal process. The results obtained are compared with several predictions. The analysis is performed as a function of the following observables:

- the transverse momentum (p_{T}) of the leading lepton,
- the p_{T} of the jet,
- the difference in the ϕ angle of the muon and the electron in the event, $\Delta\varphi(\mathrm{e}^{\pm}, \mu^{\mp})$;
- the longitudinal component of the system formed by the muon, the electron and the jet of the event, $p_{\mathrm{Z}}(\mathrm{e}^{\pm}, \mu^{\mp}, j)$;
- the invariant mass of the system formed by the electron, the muon and the jet, $m(\mathrm{e}^{\pm}, \mu^{\mp}, j)$;
- the transverse mass of the system of formed by the electron, the muon, the jet and the missing transverse momentum of the event, $m_{\mathrm{T}}(\mathrm{e}^{\pm}, \mu^{\mp}, j, p_{\mathrm{T}}^{\mathrm{miss}})$.

The first two variables provide central information regarding the kinematic properties of the events. Even more, they give another probe to the modellisation of the top quark p_{T}. The $\Delta\varphi(\mathrm{e}^{\pm}, \mu^{\mp})$ variable allows the exploration of correlations between both physical objects and explore spin-related properties. The $p_{\mathrm{Z}}(\mathrm{e}^{\pm}, \mu^{\mp}, j)$ distribution can be used to probe the boost of the complete tW system. The last two, invariant and transverse mass, permits to apprehend mass/energy related properties of the whole system.

The paper is structured as follows. Section 2 gives a summary of the CMS detector and Monte Carlo (MC) event simulation used. The object and event selection criteria are discussed in Section 3. The information regarding the signal extraction as well as the unfolding performed is given in Section 4. The sources of systematic uncertainties taken into account are described in Section 5. The results are discussed in Section 6, and a summary of the results is presented in Section 7.

2 The CMS detector and Monte Carlo simulation

The CMS detector has a superconducting solenoid in its central region of 6 m internal diameter, providing an axial magnetic field of 3.8 T. Within the solenoid volume are a silicon pixel and strip tracker (covering $0 < \phi < 2\pi$ in azimuth and $|\eta| < 2.5$ in pseudorapidity), a lead tungstate crystal electromagnetic calorimeter (ECAL), and a brass and scintillator hadron calorimeter (HCAL), each composed of a barrel and two endcap sections. These are used to identify electrons, photons, and jets. Muons are detected in gas-ionization detectors embedded in the steel flux-return yoke outside the solenoid. The detector is nearly hermetic, providing reliable measurement of the momentum imbalance in the plane transverse to the beams. A two-level trigger system selects the most interesting pp collisions for offline analysis. A more detailed description of the CMS detector, together with a definition of the coordinate system used and the relevant kinematic variables, can be found in Ref. [17].

The tW signal is simulated at NLO using POWHEG v1 [18] with the NNPDF 3.0 PDF set [19], and PYTHIA v8.205 [20] is used for parton showering and hadronization. The definition of tW production in perturbative QCD mixes with top $\mathrm{t\bar{t}}$ production at NLO [3–5]. Two schemes are proposed to describe the tW signal and to take into account this interference: ”diagram removal” (DR) [3], where all NLO diagrams which are doubly resonant, such as those in Fig. 2, are excluded from the signal definition; and ”diagram subtraction” (DS) [3, 21], in which the differential cross section is modified with a gauge-invariant subtraction term, that locally cancels the contribution of $\mathrm{t\bar{t}}$ diagrams. A comparison of the results with expectations from theory a sample of the tW process generated at NLO with MADGRAPH5_aMC@NLO v2.2.2 [22] and NNPDF 3.0 PDFs, interfaced with PYTHIA v8.205 is also provided.

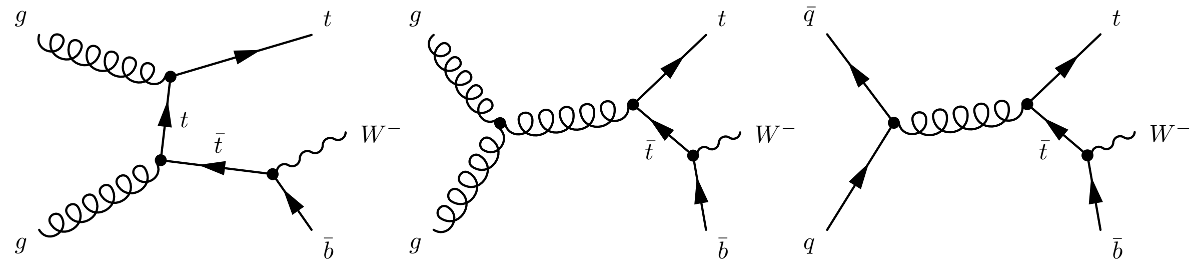

Figure 2: Feynman diagrams for tW single top quark production at NLO that are removed from the signal definition in the DR scheme, the charge-conjugate modes are implicitly included.

The NLO POWHEG v2 [23] setup is used to simulate $t\bar{t}$ events, as well as the dependency of the $t\bar{t}$ production on μ_R and μ_F, and the PDF set. The NNPDF 3.0 set is used as the default PDF set. Parton showering and hadronization for the $t\bar{t}$ events are handled by PYTHIA v8.205. Other background contributions are also estimated from MC simulations. The DY and W+jets background samples are generated at NLO with MADGRAPH5_aMC@NLO v2.2.2 [22] with NNPDF 3.0 PDFs, interfaced with PYTHIA v8.205. These processes are simulated with up to two additional partons and the FxFx scheme [24] is used for the merging. The contributions from WW, WZ, and ZZ (referred to as VV) processes are simulated at LO with PYTHIA v8.205. Other contributions from W and Z boson production in association with $t\bar{t}$ events (referred to as $t\bar{t}V$) are simulated at NLO using MADGRAPH5_aMC@NLO v2.2.2 and interfaced with PYTHIA v8.205. For all the processes except for $t\bar{t}$, the underlying event tune CUETP8M1 [25, 26] is used. For $t\bar{t}$ events the underlying event tune CUETP8M2T4 [27] is utilized. Finally, lepton+jets events in the $t\bar{t}$ and W+jets samples described above are used to estimate the contribution to the background from events with a jet incorrectly reconstructed as a lepton or with a lepton incorrectly identified as being isolated. As these last contributions to the background contain a lepton candidate that does not originate from a leptonic decay of a gauge boson, they are labeled non-W/Z.

To compare with the observed distributions, the event yields in the simulated samples are normalized using $\mathcal{L}$ and their theoretical cross sections. These are taken from NNLO for W+jets and DY [28], approximate NNLO for tW events [9]), and NLO calculations for diboson [29]. For the simulated $t\bar{t}$ sample, the full NNLO plus next-to-next-to-leading-logarithmic accuracy calculation [30], performed with the TOP++ 2.0 program [31], is used. The PDF uncertainty is added in quadrature to the uncertainty associated with the strong coupling constant (α_S) to obtain a $t\bar{t}$ production cross section of $832\,^{+20}_{-29}\,\text{(scale)} \pm 35\,(\text{PDF}+\alpha_S)$ pb assuming $m_t = 172.5\,\text{GeV}$. The simulated samples include additional interactions per bunch crossing (pileup), with the distribution matching that observed in data, with an average of 23 collisions per bunch crossing.

3 Event selection

In the SM, top quarks decay most of the times into a W boson and a bottom quark. The analysis described here uses events in the $e^{\pm}\mu^{\mp}$ final state, in which the W boson from the decay of the top quark and the W boson produced in association with the top quark both decay leptonically, one into an electron and a neutrino, and the other into a muon and another neutrino. This leads to a final state composed of two leptons with opposite charged, one jet resulting from the fragmentation of a bottom quark, and two neutrinos. The event selection used here follows closely that used in the measurement of the inclusive production cross section for single top quarks in association with W bosons [14]. Therefore, only basic requirements are given hereafter (a more detailed description can be found in Ref. [14]).

Events are required to pass either a dilepton or a single-lepton trigger. The particle-flow (PF) algorithm [32] attempts to reconstruct and identify each individual particle in an event with an optimized combination of information from the various elements of the CMS detector. Leptons (electrons [33] or muons [34]) in the event are required to be well isolated and to have $p_{\mathrm{T}} > 20\,\mathrm{GeV}$ and $|\eta| < 2.4$. Events with W bosons decaying into τ leptons are considered as signal only if the τ leptons decay into electrons or muons that satisfy the selection requirements. In events with more than two leptons passing the selection, the two with the largest p_{T} are kept for further study. Jets are reconstructed from the PF candidates using the anti-k_{T} clustering algorithm [35, 36] with a distance parameter of 0.4. Jet energy corrections, derived from simulation, are applied so that the average response to jets matches the particle-level jets [37]. In situ measurements of the momentum balance in dijet, photon+jet, Z+jet, and multijet events are used to account for any residual differences in jet energy scale (JES) between data and simulation. Jets are required to have $p_{\mathrm{T}} > 30\,\mathrm{GeV}$ and $|\eta| < 2.4$. Jets passing the above identification criteria but with p_{T} between 20 and 30 GeV are referred to as "loose jets". The missing transverse momentum vector $\vec{p}_{\mathrm{T}}^{\mathrm{miss}}$ is defined as the negative vector sum of the momenta of all reconstructed PF candidates in an event, projected onto the plane perpendicular to the direction of the beam axis. Its magnitude is referred to as $p_{\mathrm{T}}^{\mathrm{miss}}$ and the corrections to jet momenta are propagated to the $p_{\mathrm{T}}^{\mathrm{miss}}$ calculation [38]. Jets are identified as b jets using the combined secondary vertex algorithm v2 [39], with an operating point that yields identification efficiencies of $\approx$70% and misidentification (mistag) probabilities of about 1% and 15% [39] for light-flavor jets (u, d, s, and gluons) and c jets, respectively, as estimated from simulated events.

Events are considered as belonging to the $\mathrm{e}^{\pm}\mu^{\mp}$ final state if the two leptons with larger p_{T} (leading leptons) passing the above selection criteria are an electron and a muon of opposite charge. The leading lepton is required to have $p_{\mathrm{T}} > 25\,\mathrm{GeV}$. To reduce the contamination from DY production of τ lepton pairs with low invariant dilepton mass, the invariant mass of the lepton pair is required to be greater than 20 GeV. Remaining events are classifying according to the number of jets and identified b jets in the event, the most signal-enriched region is the one with one jet that is tagged as a bottom jet (1j1b region), but the size of the signal in comparison with the overwhelming $\mathrm{t\bar{t}}$ background is still tiny. To enhance the signal-to-background ratio, an additional selection criteria with respect to Ref. [14], is performed. Figure 3 shows the distribution of the number of loose jets in the events in the 1j1b region. The signal-to-background ratio is higher for events with zero loose jets. Therefore, to minimize the effect of the $\mathrm{t\bar{t}}$ background, the signal region is defined as that with events in the 1j1b region and without loose jets. The distributions of the variables under consideration for data and simulated events in the signal region are shown in Fig. 4.

4 Measurement of the differential cross section

Two different observables are considered when measuring the absolute tW differential cross section. For each variable X, the absolute differential tW cross section for a given bin i, $\left(\frac{d\sigma}{dX}\right)_{\mathrm{i}}$, can be determined using the relation:

$$\left(\frac{d\sigma}{dX}\right)_{\mathrm{i}} = \frac{1}{\mathcal{L}}\frac{N_{\mathrm{i}}^{\mathrm{sig}}}{\Delta_{\mathrm{i}}},$$

where Δ_{i} is the width of the bin and $N_{\mathrm{i}}^{\mathrm{sig}}$ is the number of expected signal events in that bin that

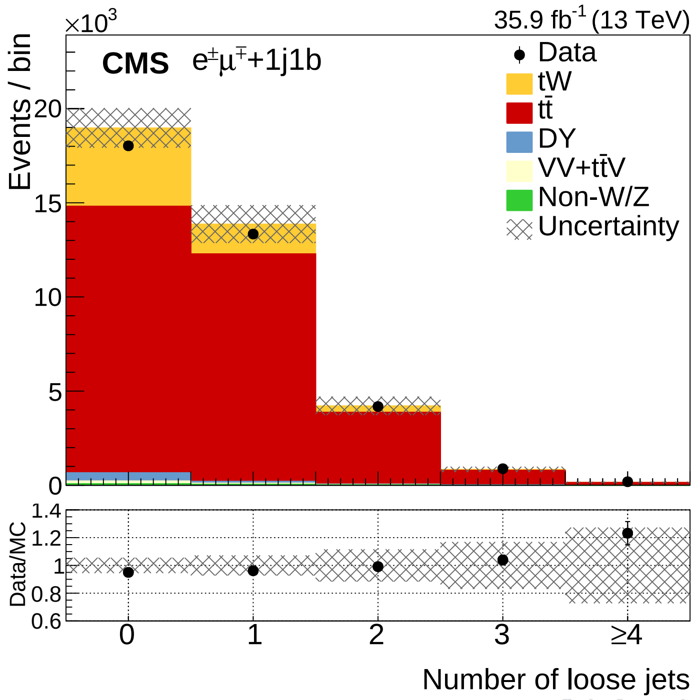

Figure 3: Yields observed in data, compared with those expected from simulation, as a function of the number of loose jets for events passing the $e^{\pm}\mu^{\mp}$ selection in the 1j1b region. The error band includes the statistical and all systematic uncertainties. The bottom of the panel shows the ratio of data to the sum of the expected yields.

can be estimated as $N_{\mathrm{i}} - N_{\mathrm{i}}^{\mathrm{bkg}}$, where N_{i} is the number of observed events in bin i and $N_{\mathrm{i}}^{\mathrm{bkg}}$ is the number of expected background events in the same bin. The measurement is performed in a fiducial region defined by the same selection requirements employed in the event selection, described in Section 3, and applied on particle-level objects. The definition of particle-level object is described in Ref. [40].

In order to take into account the migration of events among the bins of the differential cross section and outside the fiducial phase space produced by the detector response when extrapolating the results to the fiducial phase space defined by particle level objects, unfolding techniques are used. Then, for each measured variable, the response matrix (R) parameterizing the migrations among bins is constructed using the signal MC simulations. And the number of signal events in the bins of the unfolded distribution ($N_{\mathrm{j}}^{\text{sig, unf}}$) can be estimated following this expression:

$$N_{\mathrm{i}} - N_{\mathrm{i}}^{\mathrm{bkg}} = \sum_{\mathrm{j}=1} R_{\mathrm{ij}} N_{\mathrm{j}}^{\text{sig, unf}}.$$

The number of events in the unfolded space is obtained solving this equation after applying a χ^2 minimization technique. Optionally, regularization terms can be added to the χ^2 cost function in order to suppress unphysical fluctuations. In this paper, the equation is solved making use of the implementation of `TUnfold` [41]. The effect of the regularization terms has been studied in simulation and found to be not necessary.

Finally, the normalized differential cross section is obtained by dividing the absolute differential cross section by the the fiducial cross section (σ_{fid}). This ratio allows the cancelation of several systematic uncertainties to be accomplished.

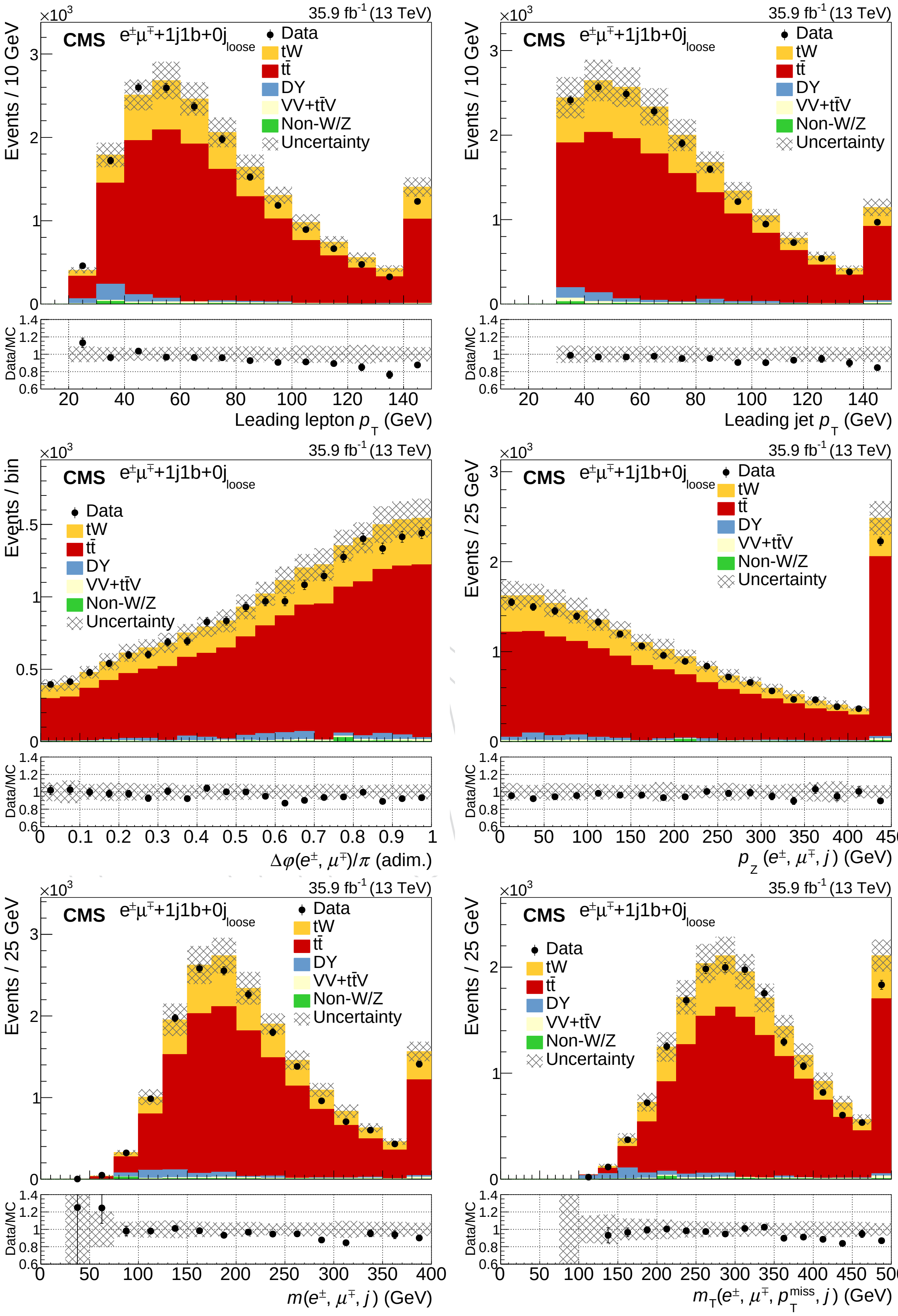

Figure 4: Yields observed in data, compared with those expected from simulation, as a function of the number of loose jets passing the dilepton selection in the signal region. The error band includes the statistical and all systematic uncertainties. The last bin of each contribution contains overflow events. The bottom of each panel shows the ratios of data to the sum of the expected yields.

5 Systematic uncertainties

The measurement of the differential tW cross sections is affected by systematic uncertainties that originate from both detector effects and theoretical assumptions. Due to the dominating presence of $\mathrm{t\bar{t}}$ events in the signal region, the impact of these uncertainty sources is mainly produced by uncertainties in the $\mathrm{t\bar{t}}$ estimation. There is a smaller contribution from experimental and theoretical uncertainties in the signal that affect to the evaluation of the response matrix used to extrapolate the measured distribution from reconstructed to particle level.

Each source of systematic uncertainty is assessed individually either by suitable variations of the MC simulations or by variations of parameter values in the analysis within their estimated uncertainties. In order to handle properly correlations of the uncertainties between signal and background, the complete analysis procedure is done with the varied simulated sample. The comparison between the nominal result and varied distribution is taken as the systematic uncertainty.

5.1 Experimental uncertainties

Uncertainties originating from detector effects affect all processes involved. The final uncertainty is taken as the difference between the nominal result and the result obtained when varying the affected parameter by its uncertainty.

Jet energy scale and resolution The uncertainty due to the limited knowledge of the JES and jet energy resolution (JER) is determined by varying the scale and resolution within the uncertainties in bins of p_{T} and η, typically by a few percent [37]. JES uncertainties are propagated to $\vec{p}_{\mathrm{T}}^{\mathrm{miss}}$.

b-tagging efficiency The uncertainties resulting from the b tagging efficiency and misidentification rate are assessed by varying, within their uncertainties, the b tagging data-to-simulation scale factors of the b jets and the light-flavor jets, respectively. These uncertainties vary with the p_{T} and η of the jet and amount to approximately 2% for b jets and 10% for mistagged jets [39], as determined in simulated $\mathrm{t\bar{t}}$ events.

Trigger and lepton identification The uncertainties in the trigger and lepton identification efficiencies in simulation are estimated by varying data-to-simulation scale factors by their uncertainties. These are about 0.7 and 1.5%, respectively, with some dependence on the lepton p_{T} and η.

Pileup The uncertainty assigned to the number of pileup events in simulation is obtained by changing the inelastic pp cross section, which is used to estimate the pileup in data, within its uncertainty of $\pm 4.6\%$ [42].

Luminosity The uncertainty on the integrated luminosity is currently estimated to be 2.5% [43].

5.2 Modeling Uncertainties

The modeling of the $\mathrm{t\bar{t}}$ and tW events by the simulation is an important ingredient in this measurement. The impact of theoretical assumptions in the modeling is determined by repeating the analysis and replacing the nominal POWHEG $\mathrm{t\bar{t}}$ and/or tW simulation by dedicated simulation samples with altered parameters. The difference in the results is taken as systematic uncertainty.

Matrix element (ME) scale The uncertainty in the modeling of the hard-production process is assessed by changing independently μ_R and μ_F in the POWHEG sample by factors of 2 and 0.5 relative to their common nominal value. This variation is performed separately for $\mathrm{t\bar{t}}$ and tW events.

Parton shower In order to take into account parton-shower (PS) uncertainties, different effects are studied:

- Underlying event: PYTHIA parameters that are tuned to the measurements of the underlying event [26, 27], to account for non-perturbative QCD effects, are varied up and down within their uncertainties in simulated $\mathrm{t\bar{t}}$ events.
- ME/PS matching: the uncertainty in the combination of the ME calculation with the parton shower in simulated $\mathrm{t\bar{t}}$ events is estimated from the variation of the POWHEG parameter $h_\mathrm{damp} = 1.58^{+0.66}_{-0.59}\ m_\mathrm{t}$ [27], which regulates the damping of real emissions in the NLO calculation when matching to the PS [26].
- Initial- (final-) state radiation scale: the PS scale used for the simulation of the initial- (final-) state radiation is varied up and down by a factor of two. These variations are motivated by the uncertainties in the PS tuning [26]. This variation is performed simultaneously for $\mathrm{t\bar{t}}$ and tW events.
- Color reconnection: the effect of multiple parton interactions and the parameterization of color reconnection have been studied in Ref. [27] and are varied accordingly in simulated $\mathrm{t\bar{t}}$ events. In addition, we use a simulation including color reconnection of early resonant decays. The uncertainties that arise from ambiguities in modeling color-reconnection effects are estimated by comparing the default model in PYTHIA with two alternative models of color reconnection, a model with string formation beyond leading color [44] and a model in which the gluons can be moved to another string [45]. All models are tuned to measurements of the underlying event [26, 27]. The largest variation in each bin with respect to the nominal yield is taken as the systematic uncertainty.

PDF The uncertainty from the choice of PDFs is determined by reweighting the sample of simulated $\mathrm{t\bar{t}}$ events according to the 100 NNPDF3.0 replicas [19]. For each bin, the root-mean-square of the variation in the acceptance for all the PDF sets is taken as an uncertainty.

5.3 Background normalization uncertainties

A normalization uncertainty of 4% [46] is used for $\mathrm{t\bar{t}}$ events. For $\mathrm{t\bar{t}V}$, VV, DY and non-W/Z background contributions, a conservative normalization uncertainty of $\pm 50\%$ is assumed, as done in Ref. [14].

6 Results

The normalized differential tW cross section as a function of the observables mentioned in Section 1 are shown in Figs. 5 and 6. Overall good agreemeent with the predcitions from POWHEG DR, POWHEG DS and MADGRAPH5_aMC@NLO is observed. The main sources of systematic uncertainty in the measurement (and their relative effect) are also shown. In general, uncertainties coming from JES and JER are the dominant ones, because of their large effect in the background estimation.

In addition, Table 1 displays the values of the χ^2 statistic and the p-values corresponding to Pearson's χ^2 goodness-of-fit test done between the observed results and the POWHEG DR, POWHEG DS and MADGRAPH5_aMC@NLO distributions. The information of the table indicates a good agreement between the expectations and the results.

Table 1: Results of the χ^2 goodness-of-fit tests performed to check the compatibility between data and the POWHEG DR, POWHEG DS and MADGRAPH5_aMC@NLO models.

	POWHEG DR	POWHEG DS	MADGRAPH5_aMC@NLO
Leading lepton p_{T}			
p-value	0.807	0.835	0.810
χ^2 statistic	0.974	0.860	0.964
Jet p_{T}			
p-value	0.851	0.876	0.876
χ^2 statistic	0.792	0.690	0.689
$\Delta\varphi(\mathrm{e}^{\pm}, \mu^{\mp})$			
p-value	0.824	0.859	0.875
χ^2 statistic	0.904	0.759	0.693
$p_{\mathrm{Z}}(\mathrm{e}^{\pm}, \mu^{\mp}, j)$			
p-value	0.965	0.965	0.962
χ^2 statistic	0.270	0.273	0.289
$m(\mathrm{e}^{\pm}, \mu^{\mp}, j)$			
p-value	0.827	0.852	0.869
χ^2 statistic	0.893	0.790	0.718
$m_{\mathrm{T}}(\mathrm{e}^{\pm}, \mu^{\mp}, j, p_{\mathrm{T}}^{\mathrm{miss}})$			
p-value	0.854	0.877	0.872
χ^2 statistic	0.779	0.684	0.705

7 Summary

The measurement of the normalized differential cross section of the production of a top quark in association with a W boson using 35.9 $\mathrm{fb}^{-1}$of data from 2016 at the CMS detector has been presented. This observable is measured as a function of various properties of the event: the p_{T} of the leading lepton, the p_{T} of the jet, the difference in the φ angle of the muon and the electron, the component in the Z axis of the muon, the electron and the jet, the invariant mass of the muon, electron and the jet, and the transverse mass of the electron, the muon, the jet, and the missing transverse momentum. The analysis is absolutely dominated by the overwhelming presence of the $\mathrm{t\bar{t}}$ process. The main sources of systematic uncertainty are related to the jet detection (i.e., jet energy resolution and jet energy scale). Modeling uncertainties of the $\mathrm{t\bar{t}}$ background are also important. The results obtained are, in general, consistent with the expectations from the two models used for the modeling of the tW signal, POWHEG and MADGRAPH5_aMC@NLO.

Acknowledgments

We congratulate our colleagues in the CERN accelerator departments for the excellent performance of the LHC and thank the technical and administrative staffs at CERN and at other CMS institutes for their contributions to the success of the CMS effort. In addition, we gratefully

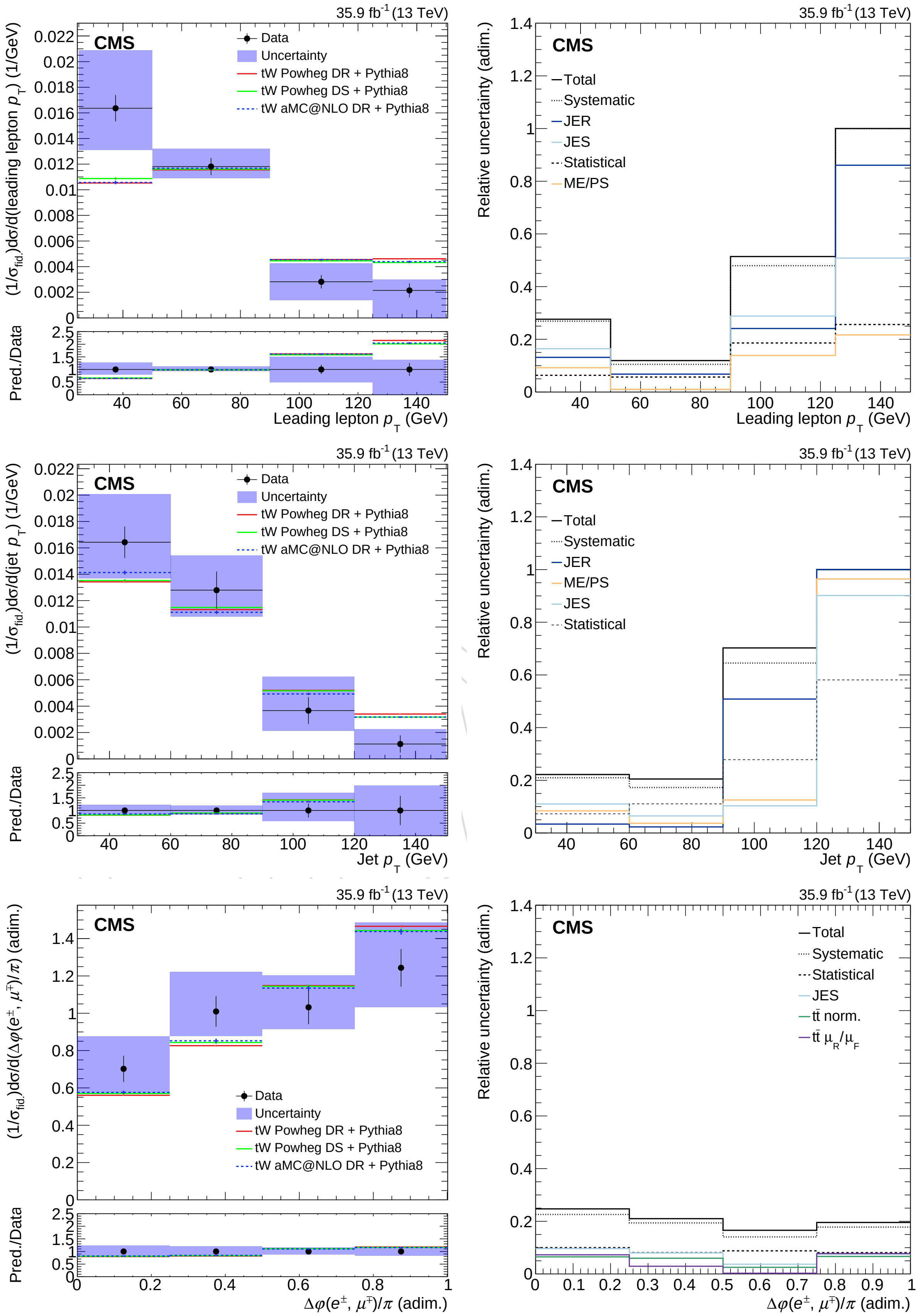

Figure 5: Left: normalized differential tW production cross section as a function of the p_T of the leading lepton (top), p_T of the jet (middle) and $\Delta\varphi(e^{\pm}, \mu^{\mp})$ (bottom) in the unfolded space. The solid band represents the total uncertainty. Predictions from POWHEG and MADGRAPH5_aMC@NLO are also shown. In the bottom panel, the ratio between data and the predictions is shown. Right: Total, systematic, statistical and individual leading relative uncertainties (averaging over all bins) as a function of each observable.

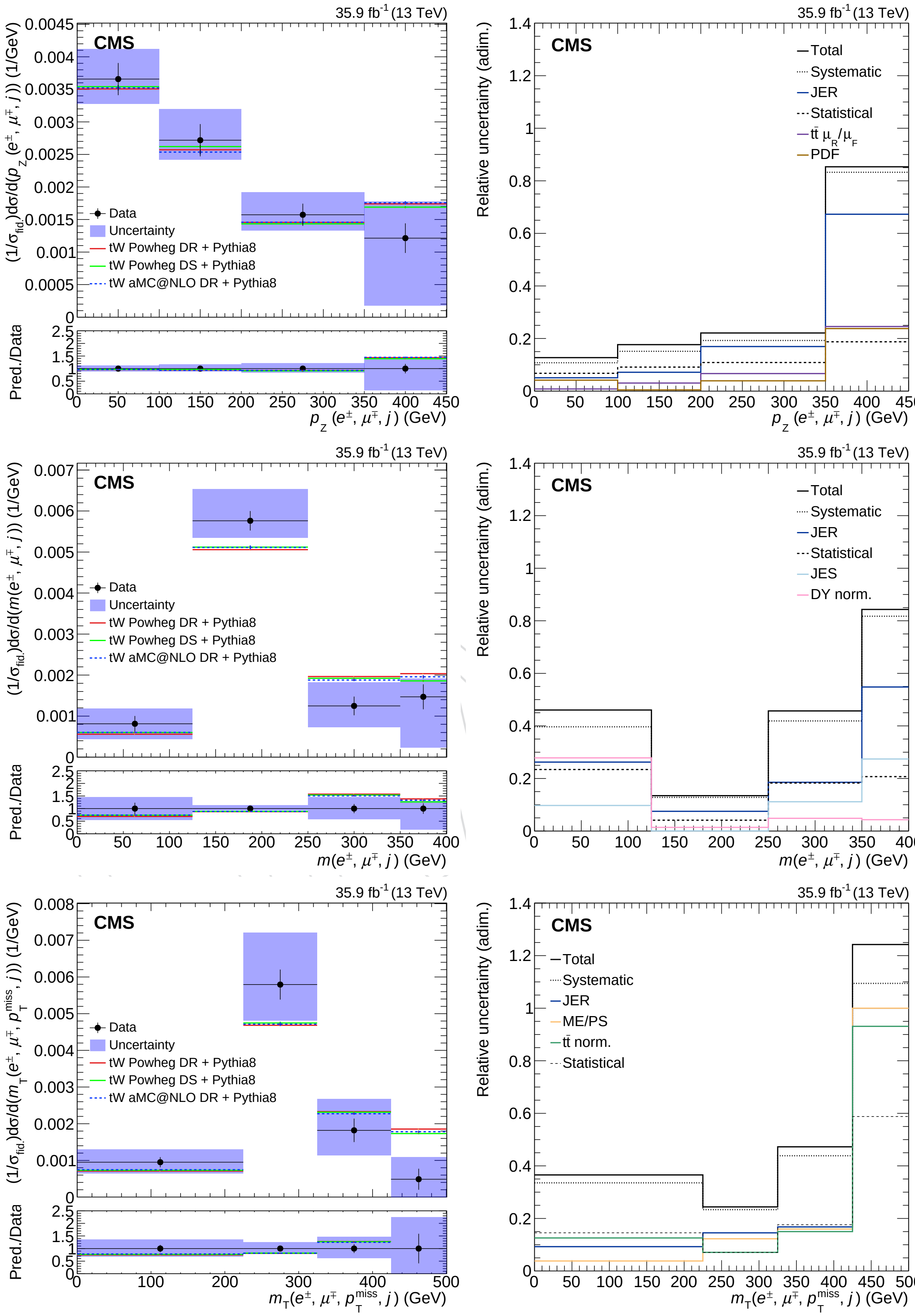

Figure 6: Left: normalized differential tW production cross section as a function of $p_Z(e^{\pm}, \mu^{\mp}, j)$ (top), $m(e^{\pm}, \mu^{\mp}, j)$ (middle) and $m_T(e^{\pm}, \mu^{\mp}, j, p_T^{miss})$ (bottom) in the unfolded space. The solid band represents the total uncertainty. Predictions from POWHEG and MADGRAPH5_aMC@NLO are also shown. In the bottom panel, the ratio between data and the predictions is shown. Right: Total, systematic, statistical and individual leading (averaging over all bins) sources of uncertainty as a function of each observable.

acknowledge the computing centres and personnel of the Worldwide LHC Computing Grid for delivering so effectively the computing infrastructure essential to our analyses. Finally, we acknowledge the enduring support for the construction and operation of the LHC and the CMS detector provided by the following funding agencies: BMBWF and FWF (Austria); FNRS and FWO (Belgium); CNPq, CAPES, FAPERJ, FAPERGS, and FAPESP (Brazil); MES (Bulgaria); CERN; CAS, MoST, and NSFC (China); COLCIENCIAS (Colombia); MSES and CSF (Croatia); RPF (Cyprus); SENESCYT (Ecuador); MoER, ERC IUT, and ERDF (Estonia); Academy of Finland, MEC, and HIP (Finland); CEA and CNRS/IN2P3 (France); BMBF, DFG, and HGF (Germany); GSRT (Greece); NKFIA (Hungary); DAE and DST (India); IPM (Iran); SFI (Ireland); INFN (Italy); MSIP and NRF (Republic of Korea); MES (Latvia); LAS (Lithuania); MOE and UM (Malaysia); BUAP, CINVESTAV, CONACYT, LNS, SEP, and UASLP-FAI (Mexico); MOS (Montenegro); MBIE (New Zealand); PAEC (Pakistan); MSHE and NSC (Poland); FCT (Portugal); JINR (Dubna); MON, RosAtom, RAS, RFBR, and NRC KI (Russia); MESTD (Serbia); SEIDI, CPAN, PCTI, and FEDER (Spain); MOSTR (Sri Lanka); Swiss Funding Agencies (Switzerland); MST (Taipei); ThEPCenter, IPST, STAR, and NSTDA (Thailand); TUBITAK and TAEK (Turkey); NASU and SFFR (Ukraine); STFC (United Kingdom); DOE and NSF (USA).

Individuals have received support from the Marie-Curie programme and the European Research Council and Horizon 2020 Grant, contract Nos. 675440 and 765710 (European Union); the Leventis Foundation; the A.P. Sloan Foundation; the Alexander von Humboldt Foundation; the Belgian Federal Science Policy Office; the Fonds pour la Formation à la Recherche dans l'Industrie et dans l'Agriculture (FRIA-Belgium); the Agentschap voor Innovatie door Wetenschap en Technologie (IWT-Belgium); the F.R.S.-FNRS and FWO (Belgium) under the "Excellence of Science – EOS" – be.h project n. 30820817; the Beijing Municipal Science & Technology Commission, No. Z181100004218003; the Ministry of Education, Youth and Sports (MEYS) of the Czech Republic; the Lendület ("Momentum") Programme and the János Bolyai Research Scholarship of the Hungarian Academy of Sciences, the New National Excellence Program ÚNKP, the NKFIA research grants 123842, 123959, 124845, 124850, 125105, 128713, 128786, and 129058 (Hungary); the Council of Science and Industrial Research, India; the HOMING PLUS programme of the Foundation for Polish Science, cofinanced from European Union, Regional Development Fund, the Mobility Plus programme of the Ministry of Science and Higher Education, the National Science Center (Poland), contracts Harmonia 2014/14/M/ST2/00428, Opus 2014/13/B/ST2/02543, 2014/15/B/ST2/03998, and 2015/19/B/ST2/02861, Sonata-bis 2012/07/E/ST2/01406; the National Priorities Research Program by Qatar National Research Fund; the Programa Estatal de Fomento de la Investigación Científica y Técnica de Excelencia María de Maeztu, grant MDM-2015-0509 and the Programa Severo Ochoa del Principado de Asturias; the Thalis and Aristeia programmes cofinanced by EU-ESF and the Greek NSRF; the Rachadapisek Sompot Fund for Postdoctoral Fellowship, Chulalongkorn University and the Chulalongkorn Academic into Its 2nd Century Project Advancement Project (Thailand); the Welch Foundation, contract C-1845; and the Weston Havens Foundation (USA).

References

[1] D0 Collaboration, "Observation of single top quark production", *Phys. Rev. Lett.* **103** (2009) 092001, doi:10.1103/PhysRevLett.103.092001, arXiv:0903.0850.

[2] CDF Collaboration, "First observation of electroweak single top quark production", *Phys. Rev. Lett.* **103** (2009) 092002, doi:10.1103/PhysRevLett.103.092002, arXiv:0903.0885.

[3] S. Frixione et al., "Single-top hadroproduction in association with a W boson", *JHEP* **07** (2008) 029, doi:10.1088/1126-6708/2008/07/029, arXiv:0805.3067.

[4] A. S. Belyaev, E. E. Boos, and L. V. Dudko, "Single top quark at future hadron colliders: Complete signal and background study", *Phys. Rev. D* **59** (1999) 075001, doi:10.1103/PhysRevD.59.075001, arXiv:hep-ph/9806332.

[5] C. D. White, S. Frixione, E. Laenen, and F. Maltoni, "Isolating Wt production at the LHC", *JHEP* **11** (2009) 074, doi:10.1088/1126-6708/2009/11/074, arXiv:0908.0631.

[6] T. M. P. Tait and C. P. Yuan, "Single top quark production as a window to physics beyond the standard model", *Phys. Rev. D* **63** (2000) 014018, doi:10.1103/PhysRevD.63.014018, arXiv:hep-ph/0007298.

[7] Q.-H. Cao, J. Wudka, and C. P. Yuan, "Search for new physics via single top production at the LHC", *Phys. Lett. B* **658** (2007) 50, doi:10.1016/j.physletb.2007.10.057, arXiv:0704.2809.

[8] V. Barger, M. McCaskey, and G. Shaughnessy, "Single top and Higgs associated production at the LHC", *Phys. Rev. D* **81** (2010) 034020, doi:10.1103/PhysRevD.81.034020, arXiv:0911.1556.

[9] N. Kidonakis, "Theoretical results for electroweak-boson and single-top production", in *Proceedings, 23rd International Workshop on Deep-Inelastic Scattering and Related Subjects (DIS 2015): Dallas, Texas, USA, April 27-May 01, 2015*, volume DIS2015, p. 170. 2015. arXiv:1506.04072.

[10] CMS Collaboration, "Evidence for associated production of a single top quark and W boson in pp collisions at $\sqrt{s} = 7$ TeV", *Phys. Rev. Lett.* **110** (2013) 022003, doi:10.1103/PhysRevLett.110.022003, arXiv:1209.3489.

[11] ATLAS Collaboration, "Evidence for the associated production of a W boson and a top quark in ATLAS at $\sqrt{s} = 7$ TeV", *Phys. Lett. B* **716** (2012) 142, doi:10.1016/j.physletb.2012.08.011, arXiv:1205.5764.

[12] CMS Collaboration, "Observation of the associated production of a single top quark and a W boson in pp collisions at $\sqrt{s} = 8$ TeV", *Phys. Rev. Lett.* **112** (2014) 231802, doi:10.1103/PhysRevLett.112.231802, arXiv:1401.2942.

[13] ATLAS Collaboration, "Measurement of the production cross-section of a single top quark in association with a W boson at 8 TeV with the ATLAS experiment", *JHEP* **01** (2016) 064, doi:10.1007/JHEP01(2016)064, arXiv:1510.03752.

[14] CMS Collaboration, "Measurement of the production cross section for single top quarks in association with W bosons in proton-proton collisions at $\sqrt{s} = 13$ TeV", *JHEP* **10** (2018) 117, doi:10.1007/JHEP10(2018)117, arXiv:1805.07399.

[15] ATLAS Collaboration, "Measurement of the cross-section for producing a W boson in association with a single top quark in pp collisions at $\sqrt{s} = 13$ TeV with ATLAS", *JHEP* **01** (2018) 063, doi:10.1007/JHEP01(2018)063, arXiv:1612.07231.

[16] ATLAS Collaboration, "Measurement of differential cross-sections of a single top quark produced in association with a W boson at $\sqrt{s} = 13$ TeV with ATLAS", *Eur. Phys. J. C* **78** (2018) 186, doi:10.1140/epjc/s10052-018-5649-8, arXiv:1712.01602.

[17] CMS Collaboration, "The CMS experiment at the CERN LHC", *JINST* **3** (2008) S08004, doi:10.1088/1748-0221/3/08/S08004.

[18] E. Re, "Single-top Wt-channel production matched with parton showers using the POWHEG method", *Eur. Phys. J. C* **71** (2011) 1547, doi:10.1140/epjc/s10052-011-1547-z, arXiv:1009.2450.

[19] NNPDF Collaboration, "Parton distributions for the LHC Run II", *JHEP* **04** (2015) 040, doi:10.1007/JHEP04(2015)040, arXiv:1410.8849.

[20] T. Sjöstrand et al., "An introduction to PYTHIA 8.2", *Comput. Phys. Commun.* **191** (2015) 159, doi:10.1016/j.cpc.2015.01.024, arXiv:1410.3012.

[21] T. M. P. Tait, "tW^- mode of single top quark production", *Phys. Rev. D* **61** (1999) 034001, doi:10.1103/PhysRevD.61.034001.

[22] J. Alwall et al., "The automated computation of tree-level and next-to-leading order differential cross sections, and their matching to parton shower simulations", *JHEP* **07** (2014) 079, doi:10.1007/JHEP07(2014)079, arXiv:1405.0301.

[23] S. Alioli, P. Nason, C. Oleari, and E. Re, "A general framework for implementing NLO calculations in shower Monte Carlo programs: the POWHEG BOX", *JHEP* **06** (2010) 043, doi:10.1007/JHEP06(2010)043, arXiv:1002.2581.

[24] R. Frederix and S. Frixione, "Merging meets matching in MC@NLO", *JHEP* **12** (2012) 061, doi:10.1007/JHEP12(2012)061, arXiv:1209.6215.

[25] CMS Collaboration, "Event generator tunes obtained from underlying event and multiparton scattering measurements", *Eur. Phys. J. C* **76** (2016) 155, doi:10.1140/epjc/s10052-016-3988-x, arXiv:1512.00815.

[26] P. Skands, S. Carrazza, and J. Rojo, "Tuning PYTHIA 8.1: the Monash 2013 Tune", *Eur. Phys. J. C* **74** (2014) 3024, doi:10.1140/epjc/s10052-014-3024-y, arXiv:1404.5630.

[27] CMS Collaboration, "Investigations of the impact of the parton shower tuning in Pythia 8 in the modelling of $\mathrm{t\bar{t}}$ at $\sqrt{s} = 8$ and 13 TeV", CMS Physics Analysis Summary CMS-PAS-TOP-16-021, CERN, 2016.

[28] Y. Li and F. Petriello, "Combining QCD and electroweak corrections to dilepton production in the framework of the FEWZ simulation code", *Phys. Rev. D* **86** (2012) 094034, doi:10.1103/PhysRevD.86.094034, arXiv:1208.5967.

[29] J. M. Campbell, R. K. Ellis, and C. Williams, "Vector boson pair production at the LHC", *JHEP* **07** (2011) 018, doi:10.1007/JHEP07(2011)018, arXiv:1105.0020.

[30] M. Czakon, P. Fiedler, and A. Mitov, "Total top-quark pair-production cross section at hadron colliders through $o(\alpha_s^4)$", *Phys. Rev. Lett.* **110** (2013) 252004, doi:10.1103/PhysRevLett.110.252004, arXiv:1303.6254.

[31] M. Czakon and A. Mitov, "Top++: A program for the calculation of the top-pair cross-section at hadron colliders", *Comput. Phys. Commun.* **185** (2014) 2930, doi:10.1016/j.cpc.2014.06.021, arXiv:1112.5675.

[32] CMS Collaboration, "Particle-flow reconstruction and global event description with the CMS detector", *JINST* **12** (2017) P10003, doi:10.1088/1748-0221/12/10/P10003, arXiv:1706.04965.

[33] CMS Collaboration, "Performance of electron reconstruction and selection with the CMS detector in proton-proton collisions at $\sqrt{s} = 8\,\text{TeV}$", *JINST* **10** (2015) P06005, doi:10.1088/1748-0221/10/06/P06005, arXiv:1502.02701.

[34] CMS Collaboration, "Performance of CMS muon reconstruction in pp collision events at $\sqrt{s} = 7$ TeV", *JINST* **7** (2012) P10002, doi:10.1088/1748-0221/7/10/P10002, arXiv:1206.4071.

[35] M. Cacciari, G. P. Salam, and G. Soyez, "The anti-k_{T} jet clustering algorithm", *JHEP* **04** (2008) 063, doi:10.1088/1126-6708/2008/04/063, arXiv:0802.1189.

[36] M. Cacciari, G. P. Salam, and G. Soyez, "FastJet user manual", *Eur. Phys. J. C* **72** (2012) 1896, doi:10.1140/epjc/s10052-012-1896-2, arXiv:1111.6097.

[37] CMS Collaboration, "Jet algorithms performance in 13 TeV data", CMS Physics Analysis Summary CMS-PAS-JME-16-003, CERN, 2017.

[38] CMS Collaboration, "Performance of missing energy reconstruction in $\sqrt{s} = 13$ TeV pp collision data using the CMS detector", CMS Physics Analysis Summary CMS-PAS-JME-16-004, CERN, 2016.

[39] CMS Collaboration, "Identification of heavy-flavour jets with the CMS detector in pp collisions at 13 TeV", *JINST* **13** (2018) P05011, doi:10.1088/1748-0221/13/05/P05011, arXiv:1712.07158.

[40] CMS Collaboration, "Object definitions for top quark analyses at the particle level", Technical Report CMS-NOTE-2017-004, CERN, Geneva, 2017.

[41] S. Schmitt, "TUnfold: an algorithm for correcting migration effects in high energy physics", *JINST* **7** (2012) T10003, doi:10.1088/1748-0221/7/10/T10003, arXiv:1205.6201.

[42] ATLAS Collaboration, "Measurement of the inelastic proton-proton cross section at $\sqrt{s} = 13$ TeV with the ATLAS detector at the LHC", *Phys. Rev. Lett.* **117** (2016) 182002, doi:10.1103/PhysRevLett.117.182002, arXiv:1606.02625.

[43] CMS Collaboration, "CMS luminosity measurements for the 2016 data taking period", CMS Physics Analysis Summary CMS-PAS-LUM-17-001, CERN, 2017.

[44] J. R. Christiansen and P. Z. Skands, "String formation beyond leading colour", *JHEP* **08** (2015) 003, doi:10.1007/JHEP08(2015)003, arXiv:1505.01681.

[45] S. Argyropoulos and T. Sjöstrand, "Effects of color reconnection on $\mathrm{t\bar{t}}$ final states at the LHC", *JHEP* **11** (2014) 043, doi:10.1007/JHEP11(2014)043, arXiv:1407.6653.

[46] CMS Collaboration, "Measurement of the $\mathrm{t\bar{t}}$ production cross section, the top quark mass, and the strong coupling constant using dilepton events in pp collisions at $\sqrt{s} = 13$ TeV", arXiv:1812.10505.

A Supplemental material

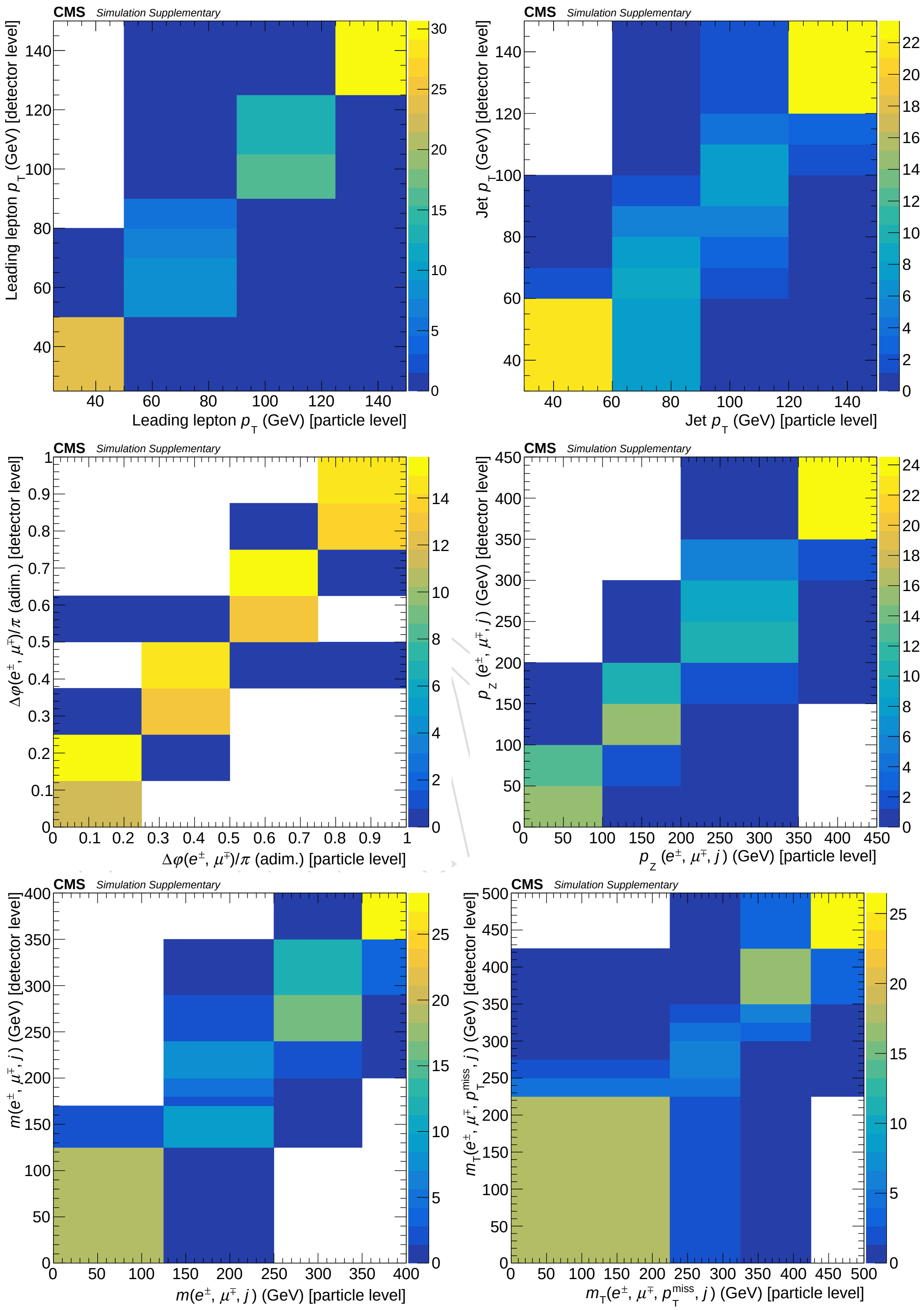

Figure 7: Response matrices of the variables under study: the reconstructed event axis is the folded space axis and the generated event axis, the unfolded. They are scaled to 100 (all contents multiplied by it).

Table 2: Numerical results of the normalized differential cross sections for all the observables considered, as well as the upper and lower uncertainties for each case.

Leading lepton p_{T} (GeV)	[25, 50)	[50, 90)	[90, 125)	[125, ∞)
$d\sigma/d$ (Leading lepton p_{T}) (1/ GeV)	0.016	0.0118	0.003	0.0021
Upper unc. (1/ GeV)	0.005	0.0014	0.001	0.0008
Lower unc. (1/ GeV)	0.003	0.0009	0.001	0.0025
Jet p_{T} (GeV)	[30, 60)	[60, 90)	[90, 120)	[120, ∞)
$d\sigma/d$ (Jet p_{T}) (1/ GeV)	0.016	0.013	0.004	0.0011
Upper unc. (1/ GeV)	0.004	0.003	0.003	0.0011
Lower unc. (1/ GeV)	0.003	0.002	0.002	0.0038
$\Delta\varphi(\mathrm{e}^{\pm},\mu^{\mp})/\ \pi$ (adim.)	[0, 0.25)	[0.25, 0.50)	[0.50, 0.75)	[0.75, 1]
$d\sigma/d$ ($\Delta\varphi(\mathrm{e}^{\pm},\mu^{\mp})/\pi$) (adim.)	0.7	1.0	1.0	1.2
Upper unc. (adim.)	0.2	0.2	0.2	0.2
Lower unc. (adim.)	0.1	0.1	0.1	0.2
$p_{\mathrm{Z}}(\mathrm{e}^{\pm},\mu^{\mp},j)$ (GeV)	[0, 100)	[100, 200)	[200, 350)	[350, ∞)
$d\sigma/d$ ($p_{\mathrm{Z}}(\mathrm{e}^{\pm},\mu^{\mp},j)$) (1/ GeV)	0.0037	0.0027	0.0016	0.0012
Upper unc. (1/ GeV)	0.0005	0.0005	0.0003	0.0006
Lower unc. (1/ GeV)	0.0004	0.0003	0.0002	0.0010
$m(\mathrm{e}^{\pm},\mu^{\mp},j)$ (GeV)	[0, 125)	[125, 250)	[250, 350)	[350, ∞)
$d\sigma/d$ ($m(\mathrm{e}^{\pm},\mu^{\mp},j)$) (1/ GeV)	0.0008	0.0058	0.0012	0.0015
Upper unc. (1/ GeV)	0.0004	0.0008	0.0006	0.0004
Lower unc. (1/ GeV)	0.0004	0.0004	0.0005	0.0012
$m_{\mathrm{T}}(\mathrm{e}^{\pm},\mu^{\mp},j,p_{\mathrm{T}}^{\mathrm{miss}})$ (GeV)	[0, 225)	[225, 325)	[325, 425)	[425, ∞)
$d\sigma/d\left(m_{\mathrm{T}}(\mathrm{e}^{\pm},\mu^{\mp},j,p_{\mathrm{T}}^{\mathrm{miss}})\right)$ (1/ GeV)	0.0010	0.0058	0.00182	0.0005
Upper unc. (1/ GeV)	0.0003	0.0014	0.00009	0.0006
Lower unc. (1/ GeV)	0.0003	0.0010	0.00068	0.0014

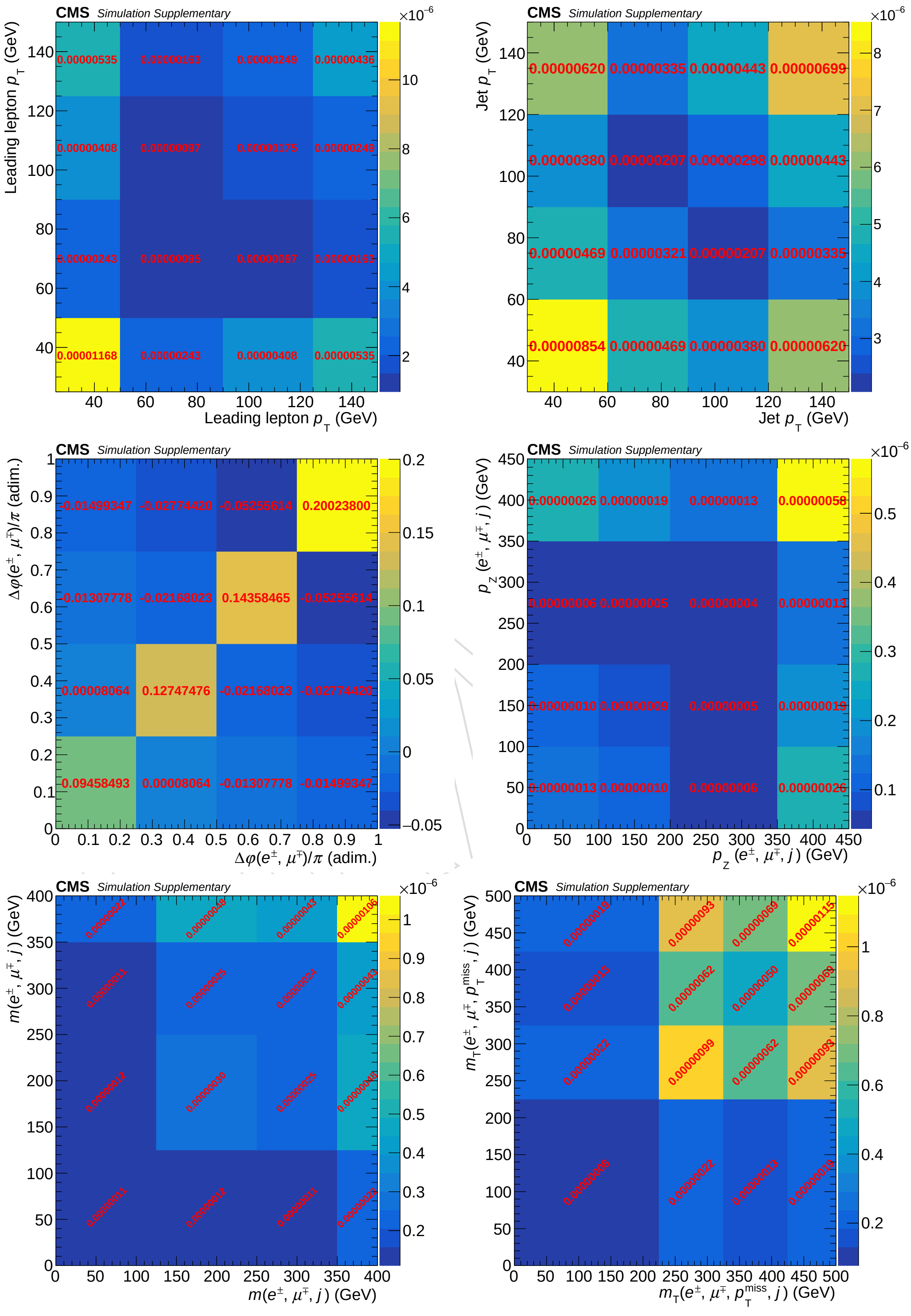

Figure 8: Covariance matrices between bins of the various observables taking into consideration all the contributions from all uncertainty sources for the final (normalised to the fiducial cross section and bin width) results.

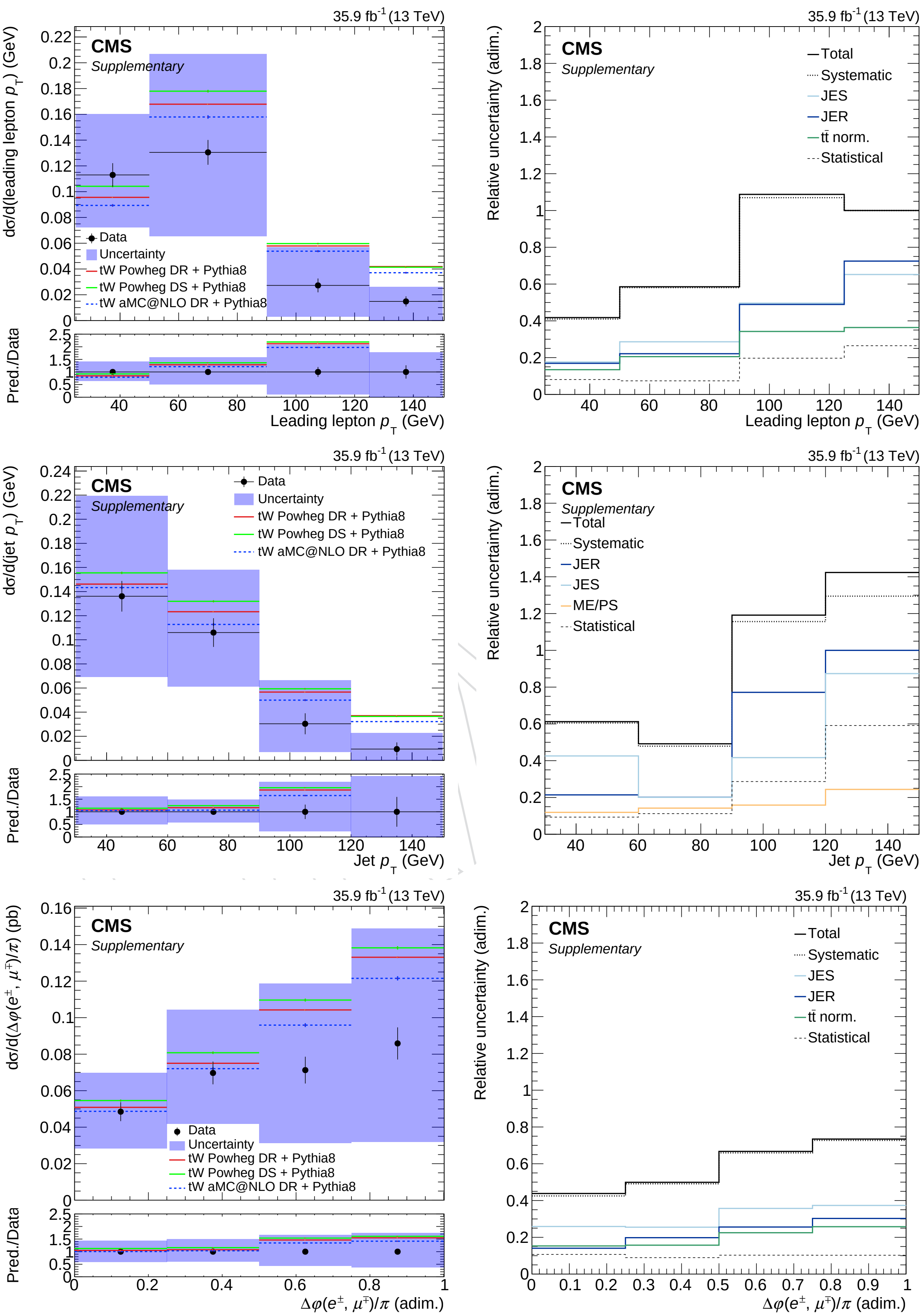

Figure 9: Left: absolute differential tW production cross section as a function of the p_T of the leading lepton (top), p_T of the jet (middle) and $\Delta\varphi(e^{\pm}, \mu^{\mp})$ (bottom) in the unfolded space. The solid band represents the total uncertainty. Predictions from POWHEG and MADGRAPH5_aMC@NLO are also shown. In the bottom panel, the ratio between data and the predictions is shown. Right: Total, systematic, statistical and individual leading relative uncertainties (averaging over all bins) as a function of each observable.

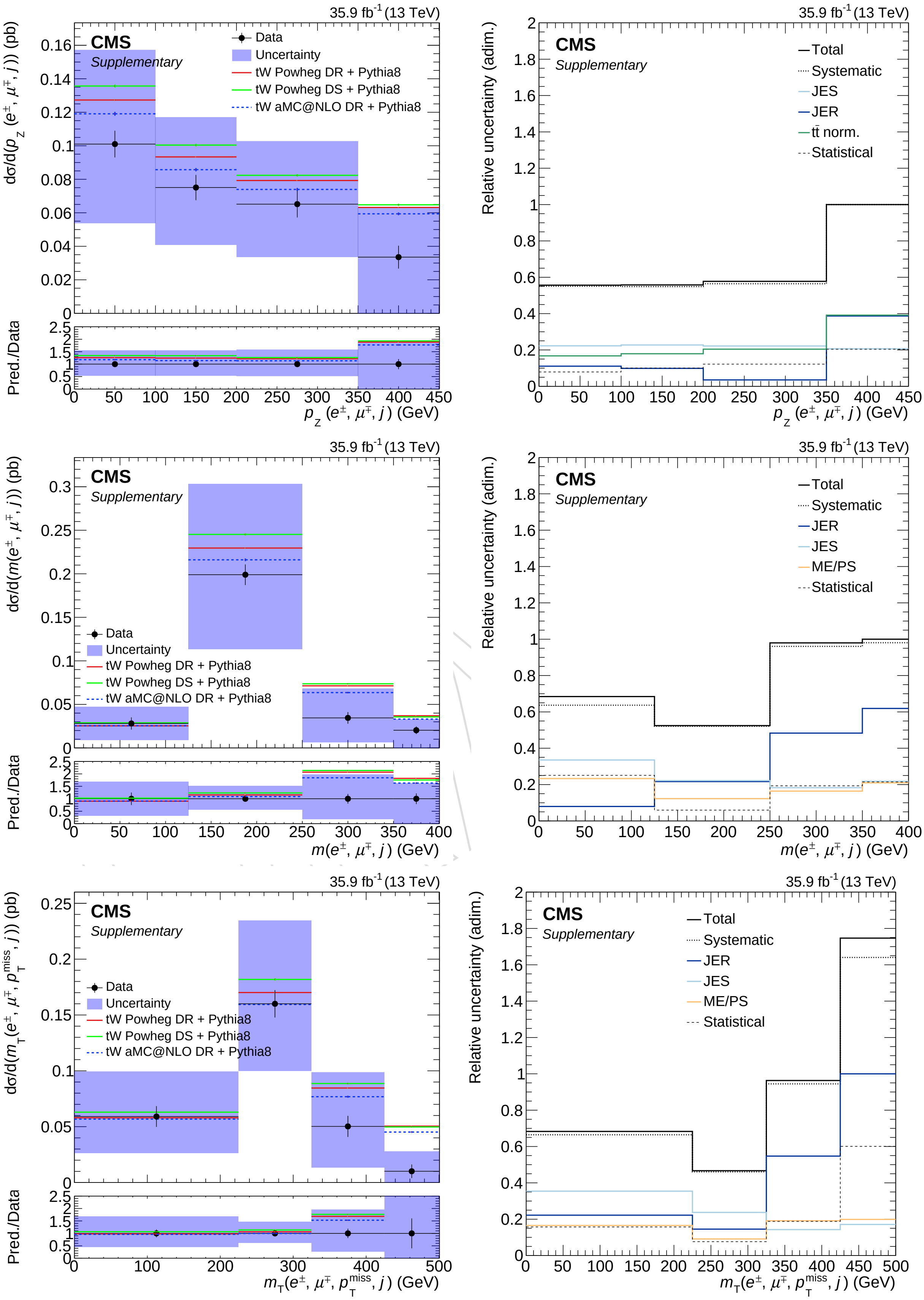

Figure 10: Left: absolute differential tW production cross section as a function of $p_Z(e^{\pm}, \mu^{\mp}, j)$ (top), $m(e^{\pm}, \mu^{\mp}, j)$ (middle) and $m_T(e^{\pm}, \mu^{\mp}, j, p_T^{miss})$ (bottom) in the unfolded space. The solid band represents the total uncertainty. Predictions from POWHEG and MADGRAPH5_aMC@NLO are also shown. In the bottom panel, the ratio between data and the predictions is shown. Right: Total, systematic, statistical and individual leading relative uncertainties (averaging over all bins) as a function of each observable.

Table 3: Numerical results of the absolute differential cross sections for all the observables considered, as well as the upper and lower uncertainties for each case.

Leading lepton p_{T} (GeV)	[25, 50)	[50, 90)	[90, 125)	[125, ∞)
$d\sigma/d$ (Leading lepton p_{T}) (pb)	0.11	0.13	0.03	0.015
Upper unc. (pb)	0.05	0.08	0.03	0.012
Lower unc. (pb)	0.04	0.06	0.02	0.019
Jet p_{T} (GeV)	[30, 60)	[60, 90)	[90, 120)	[120, ∞)
$d\sigma/d$ (Jet p_{T}) (pb)	0.14	0.11	0.03	0.009
Upper unc. (pb)	0.08	0.05	0.04	0.013
Lower unc. (pb)	0.07	0.04	0.02	0.033
$\Delta\varphi(\mathrm{e}^{\pm}, \mu^{\mp})/\ \pi$	[0, 0.25)	[0.25, 0.50)	[0.50, 0.75)	[0.75, 1]
$d\sigma/d$ ($\Delta\varphi(\mathrm{e}^{\pm}, \mu^{\mp})/\pi$) (pb)	0.05	0.07	0.07	0.09
Upper unc. (pb)	0.02	0.04	0.05	0.06
Lower unc. (pb)	0.02	0.03	0.04	0.05
$p_{\mathrm{Z}}(\mathrm{e}^{\pm}, \mu^{\mp}, j)$ (GeV)	[0, 100)	[100, 200)	[200, 350)	[350, ∞)
$d\sigma/d$ ($p_{\mathrm{Z}}(\mathrm{e}^{\pm}, \mu^{\mp}, j)$) (pb)	0.10	0.08	0.07	0.03
Upper unc. (pb)	0.06	0.04	0.04	0.03
Lower unc. (pb)	0.05	0.03	0.03	0.03
$m(\mathrm{e}^{\pm}, \mu^{\mp}, j)$ (GeV)	[0, 125)	[125, 250)	[250, 350)	[350, ∞)
$d\sigma/d$ ($m(\mathrm{e}^{\pm}, \mu^{\mp}, j)$) (pb)	0.03	0.20	0.03	0.02
Upper unc. (pb)	0.02	0.10	0.03	0.01
Lower unc. (pb)	0.02	0.08	0.03	0.02
$m_{\mathrm{T}}(\mathrm{e}^{\pm}, \mu^{\mp}, j, p_{\mathrm{T}}^{\mathrm{miss}})$ (GeV)	[0, 225)	[225, 325)	[325, 425)	[425, ∞)
$d\sigma/d$ $\left(m_{\mathrm{T}}(\mathrm{e}^{\pm}, \mu^{\mp}, j, p_{\mathrm{T}}^{\mathrm{miss}})\right)$ (pb)	0.06	0.16	0.05	0.010
Upper unc. (pb)	0.04	0.07	0.05	0.018
Lower unc. (pb)	0.03	0.06	0.03	0.027

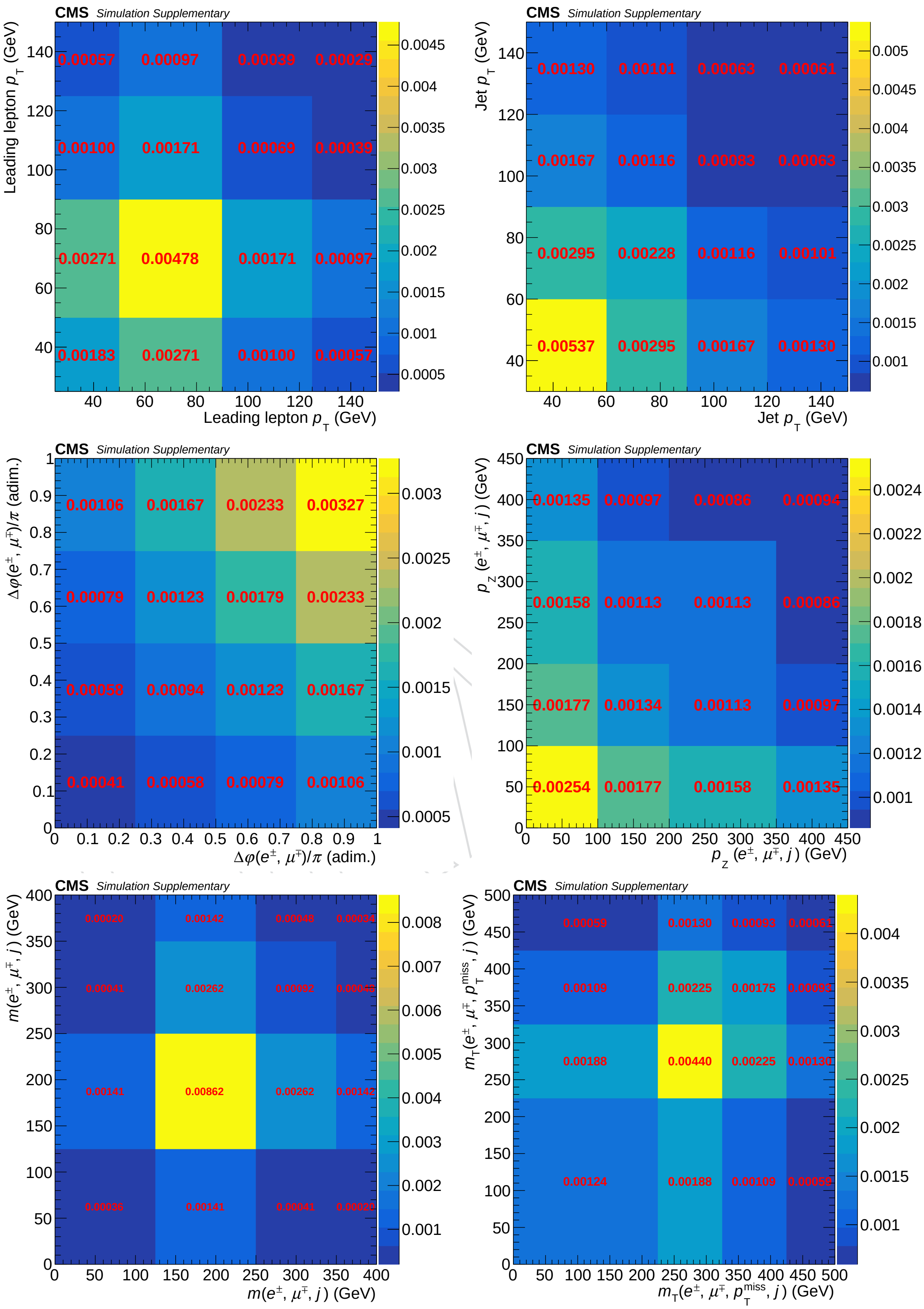

Figure 11: Covariance matrices between bins of the various observables taking into consideration all the contributions from all uncertainty sources for the absolute results obtained after unfolding.